Available online at www.sciencedirect.com
ScienceDirect
Journal of Nuclear Materials 358 (2006) 227–234
journal of nuclear materials
www.elsevier.com/locate/jnucmat

Corrosion of ferritic–martensitic steel HT9 in supercritical water

X. Ren [a,*], K. Sridharan [b], T.R. Allen [a,b]

[a] Materials Science Program, University of Wisconsin, 1415 Engineering Dr., Madison, WI 53706, USA
[b] Department of Engineering Physics, University of Wisconsin, 1500 Engineering Dr., Madison, WI 53706, USA

Received 11 October 2005; accepted 7 July 2006

Abstract

The oxidation of a 12% Cr ferritic–martensitic steel, HT9 has been examined after exposure to supercritical water (SCW) at 500 °C with two different dissolved oxygen contents, 25 wppb and 2 wppm, for exposure periods of up to 505 h. Samples exposed to the higher oxygen content SCW showed Cr-rich blades and generally a much finer oxide grain structure than samples exposed to the lower oxygen content SCW which have a porous surface oxide structure. A double-layer oxide structure developed on all samples exposed in 25 wppb oxygen content SCW, consisting specifically of an Fe-rich outer magnetite layer and a Cr-rich inner oxide layer composed of spinel and ferrite. An outer hematite layer was also found for samples exposed to 2 wppm oxygen content SCW. Samples whose surface was pre-implanted with oxygen and then exposed to SCW with 25 wppb oxygen content for 505 h showed a slightly lower weight gain compared to the untreated samples. This difference in weight gain appears to be associated with a preferred orientation in the outer oxide layer.

PACS: 81.65.Mq; 82.33.De; 52.77.Dq; 68.37.Hk; 61.82.Bg

1. Introduction

The supercritical water reactor (SCWR) design has been selected as one of the reactor concepts for future Generation IV nuclear reactor systems, because of its simplified design, smaller volume, and higher thermal efficiency than current light water reactors (LWRs) [1]. Supercritical water (SCW) coolant continues to be an attractive choice for fossil fuel power plants owing to its ability to be used at higher temperature and pressure with associated higher thermal efficiency [2]. Above the thermodynamic critical point (374.2 °C temperature and 22.1 MPa pressure), SCW acts as a dense gas, whose properties, such as density, ion product and dielectric constant, can be tuned by adjusting the temperature and pressure to meet the requirements of different applications [3]. However, SCW is expected to be more corrosive to structural materials that are commonly used in nuclear reactors and fossil power plants. Therefore, the corrosion behavior, including oxidation kinetics, oxide structure, and oxide phases, of candidate materials for the SCWR have to be thoroughly investigated prior to its safe application in nuclear reactor systems and other applications. Ferritic–martensitic (F/M) steels,

* Corresponding author. Tel.: +1 608 262 3437; fax: +1 608 263 7451.
E-mail address: xiaoweiren@wisc.edu (X. Ren).

0022-3115/$ - see front matter © 2006 Elsevier B.V. All rights reserved.
doi:10.1016/j.jnucmat.2006.07.010

nickel-based alloys, austenitic stainless steels and oxide-dispersion strengthened (ODS) alloys are considered as candidates for future SCWR systems [4]. Among these classes of alloys, austenitic steels generally have lower thermal conductivity, higher coefficient of thermal expansion, higher density, and poorer weldability. The high-temperature Ni-based alloys also have lower thermal conductivity, and increased cost. More importantly, these two categories of alloys contain substantial amounts of Ni, which is susceptible to transmutation under the influence of radiation [1]. Consequently, relatively low Ni or Ni-free ferritic–martensitic steels present an attractive choice; however, their corrosion performance under SCW temperatures and pressures is the subject of continuing research.

Ferritic–martensitic steels with chromium contents between 9 and 12 wt% and low nickel content have attracted increasing attention because of their high creep-rupture strength combined with good oxidation and corrosion resistance at elevated temperatures [5]. Owing to its proven resistance to high radiation dose, HT9 has been used for fuel cladding and other structural components in the US fast reactor program [6]. HT9 is also used for superheater tubes, steam pipes, and thick-section boiler headers in fossil plants. In this alloy, tungsten and molybdenum are added in small quantities for solid solution strengthening, while vanadium is added for precipitation hardening by the formation of fine nitride phase particles [5]. Research on the oxidation behavior of 9–12% Cr ferritic–martensitic steels in a steam environment at temperatures of up to 700 °C has been reviewed by Wright and Pint [2] and Fry et al. [7]. However, relatively few oxidation studies have been conducted in the temperature and pressure domain corresponding to supercritical conditions [8–10]. The work described in this paper investigates the corrosion performance of HT9 exposed to SCW at 500 °C under a pressure of 25 MPa for time periods up to 505 h and represents a part of the ongoing research program at the University of Wisconsin on testing and screening of a wide range of alloys for future SCWR systems.

2. Experimental

The actual chemical composition in weight percent of HT9 is listed in Table 1. The HT9 samples used in this study were procured from excess reactor components (specifically hexagonal ducts) from the Experimental Breeder Reactor (EBR-II) program. The as-received bulk HT9 was cut into coupons of dimension 31.75 mm × 12.7 mm × 0.34–0.49 mm, and then mechanically polished to a one-micron diamond paste finish before SCW exposure. All SCW exposure tests were performed at a temperature of 500 °C under a pressure of 25 MPa with a flow rate of around 1 m/s [11]. To study the influence of dissolved oxygen concentration in SCW on the corrosion behavior of alloys, two tests were conducted at different dissolved oxygen content, 25 wppb and 2 wppm, respectively. While the lower oxygen content (25 wppb) is more representative of the operating conditions in SCW-based nuclear reactors, the higher oxygen content of 2 wppm was investigated to simulate conditions that might be encountered due to radiolysis of SCW. The exposure times were 172, 333, 505 h for the 25 wppb test, and 168, 335 and 503 h for the 2 wppm test. In each test, the samples exposed for short exposure times (about 170 and 334 h) were taken out after designed exposure times. The samples with the longest exposure time were cooled down to the room temperature once during the test (as part of a sample exchange) and reheated to 500 °C to achieve the designed exposure time. In addition, some HT9 samples ion implanted with oxygen using plasma source ion implantation (PSII) were tested in the 25 wppb SCW to explore the effects of this surface treatment on corrosion performance of HT9 in SCW environment. Oxygen ions were implanted into the surface at an energy of about 40 kV to a dose of 3×10^{21} ions/m^2. The depth of the modified region was approximately 0.15 μm and the peak oxygen concentration was about 20–25 at%.

All the samples were weighed using a SCIENTECH SA-80 Milligram Balance with an accuracy of 0.1 mg prior to and after exposure to SCW, to monitor the weight change due to oxidation. To

Table 1
Actual chemical composition (in wt%) of alloy HT9 used in this study

Alloy	Fe	Cr	Ni	W	Mo	Mn	Si	V	C	Other
HT9	84.36	11.94	0.62	0.48	1.03	0.69	0.30	0.30	0.21	S_0.005, P_0.013, Cu_0.02, Co_0.03, N_0.005, Al_ < 0.01, Ti_ < 0.01

minimize the random measurement error, every measurement was repeated four times, and the arithmetical average value is reported. A Hitachi JEO JSM-6100 scanning electron microscope (SEM), equipped with energy dispersive X-ray spectroscopy (EDS), was used to investigate the oxide morphology, chemical composition and oxide thickness. The determination of grain orientation distribution and phase identification were performed using a LEO-1530 SEM equipped with electron backscattering diffraction (EBSD) capability, and a STOE X-ray diffraction (XRD) system, respectively.

3. Results and discussion

The weight gain data of HT9 exposed to SCW with the two levels of dissolved oxygen for various exposure periods at 500 °C are shown in Fig. 1. Since the testing time (several weeks) is much shorter than the service lifetime (tens of years) of nuclear reactors or fossil power plants, an extrapolation based on fitting available experimental data was performed to provide an idea of trends in oxide growth at prolonged exposures. The experimental weight gain (WG) data can be fitted using the following equations:

$$WG = Ae^{Q/kT}t^n = A't^n, \quad (1)$$

where A and A' are constants, Q is the activation energy for oxidation, T is the temperature in Kelvin, t is the exposure time, k is the Boltzmann constant, and n is the time exponent. The fitting curves and corresponding time exponents for each set of weight gain data are also shown in Fig. 1, recognizing that the trends are based on a very limited data set. Among three sets of weight change data, the 2 wppm dissolved oxygen test showed the largest weight gain throughout the exposure, and exhibited parabolic growth kinetics ($n = 0.44$). The primary reason for the larger weight gain in this case is the higher oxygen chemical potential near the materials' surface. For the 25 wppb dissolved oxygen test, the growth kinetics were closer to linear ($n = 0.72$) for untreated samples, and parabolic ($n = 0.46$) for surface modified samples. Compared to untreated samples, surface modified samples showed a slightly lower weight gain, for long exposure time (505 h), even though, the surface modified samples exhibited a slightly higher weight gain for shorter exposure times.

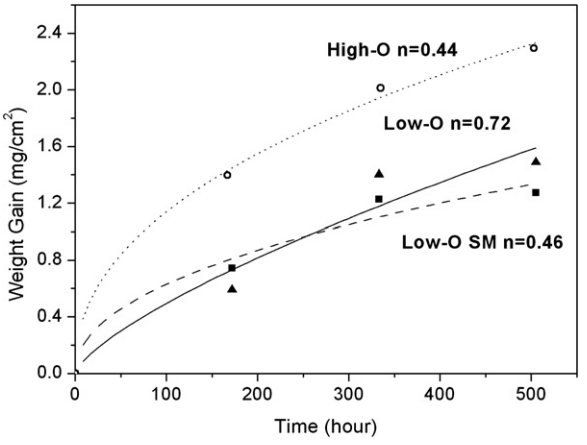

Fig. 1. Weight change data as a function of exposure time for untreated and surface modified (SM) HT9 samples after exposure to SCW with two different oxygen concentrations (25 wppb and 2 wppm) at 500 °C. 'n' values for each curve were obtained by fitting the experimental weight gain using Eq. (1).

The surface morphology of the oxide layer on the samples after SCW exposure is shown by SEM plan-view images (Fig. 2). A porous oxide structure was observed on the surface of the untreated and surface modified samples exposed to 25 wppb dissolved oxygen SCW, and the pore density was noted to increase with exposure time. These pores are likely to act as pathways for the transportation of oxygen [12]. In contrast, samples exposed to 2 wppm oxygen SCW exhibited a much finer grain size and oxide blades perpendicular to the surface. The oxide blades were identified to be Cr-rich by SEM-EDS analysis. When the exposure time increased from 168 to 503 h, the density of these Cr-rich blades also increased. The formation of such Cr-rich blades is most likely due to chromium that diffused from the bulk material through the oxide layers, driven by the high chemical potential of oxygen at the SCW/oxide interface [13]. There was no obvious oxide exfoliation observed for any of the tested samples.

Fig. 3 shows the SEM images of the cross-section of the oxide layers that formed on the untreated samples exposed to 25 wppb (Fig. 3(a)) and 2 wppm (Fig. 3(b)) dissolved oxygen SCW for about 500 h at 500 °C. The corresponding chemical composition profiles across the thickness of the oxide layers are shown below the images. Based on the morphology and elemental concentration distribution, the oxide scale of the 25 wppb SCW exposed sample can be divided into two distinct layers, an Fe-rich outer oxide layer and a Cr-rich inner oxide layer. The Fe-rich outer layer had a larger grain size (about

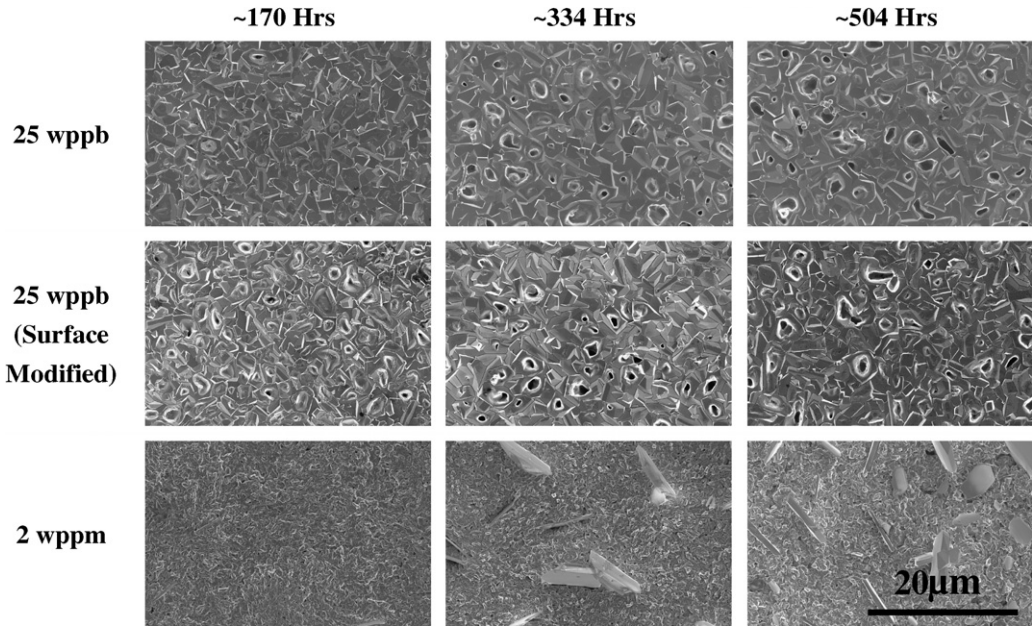

Fig. 2. SEM plan-view images of the oxide layer for untreated and surface modified HT9 samples exposed to SCW at two different dissolved oxygen contents at 500 °C for various exposure times. Cr-rich blades were identified on the surface of the samples exposed in SCW with 2 wppm dissolved oxygen content by SEM-EDS analysis.

several microns) than the Cr-rich inner layer (less than 1 μm). Additionally, a thin layer in the bulk alloy close to the oxide/metal interface was also observed. This layer represents a diffusion or internal oxidation layer, because chemical composition across this layer varied gradually from oxide to bulk alloy concentration. SEM-EDS analysis qualitatively showed that minor elements, molybdenum and tungsten were enriched in the inner oxide layer, whereas nickel was concentrated at the interface between oxide and metal. The distribution of these elements could be partially attributed to their different affinities for oxygen [14]. For example, since the oxygen affinity for Cr is larger than that of Fe, it will oxidize more readily by reacting with diffused oxygen to form a Cr-rich inner oxide layer. Simultaneously, the formation of this layer will lower the oxygen potential at the oxide/metal interface making iron oxides less stable [15]. With the growth of this layer, it will decrease the diffusion rate in it and subsequently hamper further development of scale, acting as a barrier against the diffusion of metal and oxygen ions [16]. These are the key reasons for the high corrosion resistance resulting from chromium additions to iron-based alloys [7]. Because of its lowest oxygen affinity of all elements in HT9, Ni is the least likely to be oxidize and will be concentrated at the interface between oxide and metal. Mo and W, which have similar oxide formation energies to iron [17], were only enriched in the inner oxide layer, emphasizing the relative immobility of these two elements in the magnetite. Even though samples exposed for different durations have different oxide thicknesses, similar trends regarding the double-layered oxide structure and elemental distribution were observed in all samples exposed to 25 wppb dissolved oxygen SCW, with and without surface modification. The samples exposed to 2 wppm SCW had an oxide structure and chemical composition distribution similar to the 25 wppb SCW exposed samples. The only difference in the oxide compositions between the two cases is minor enrichment of chromium close to the surface of sample exposed to 2 wppm SCW, which was mainly caused by the Cr-rich blades on sample surfaces, clearly shown by the SEM plan-view images in Fig. 2.

By capturing and analyzing the electron backscattered Kikuchi patterns from a crystalline sample, an EBSD system can be used to provide a complete and quantitative representation of the microstructure, including crystal structure, orientations and perfection, grain morphology, orientation and boundaries [18]. Fig. 4(a) and (b) shows the EBSD patterns for untreated and surface modified samples exposed to 25 wppb dissolved oxygen

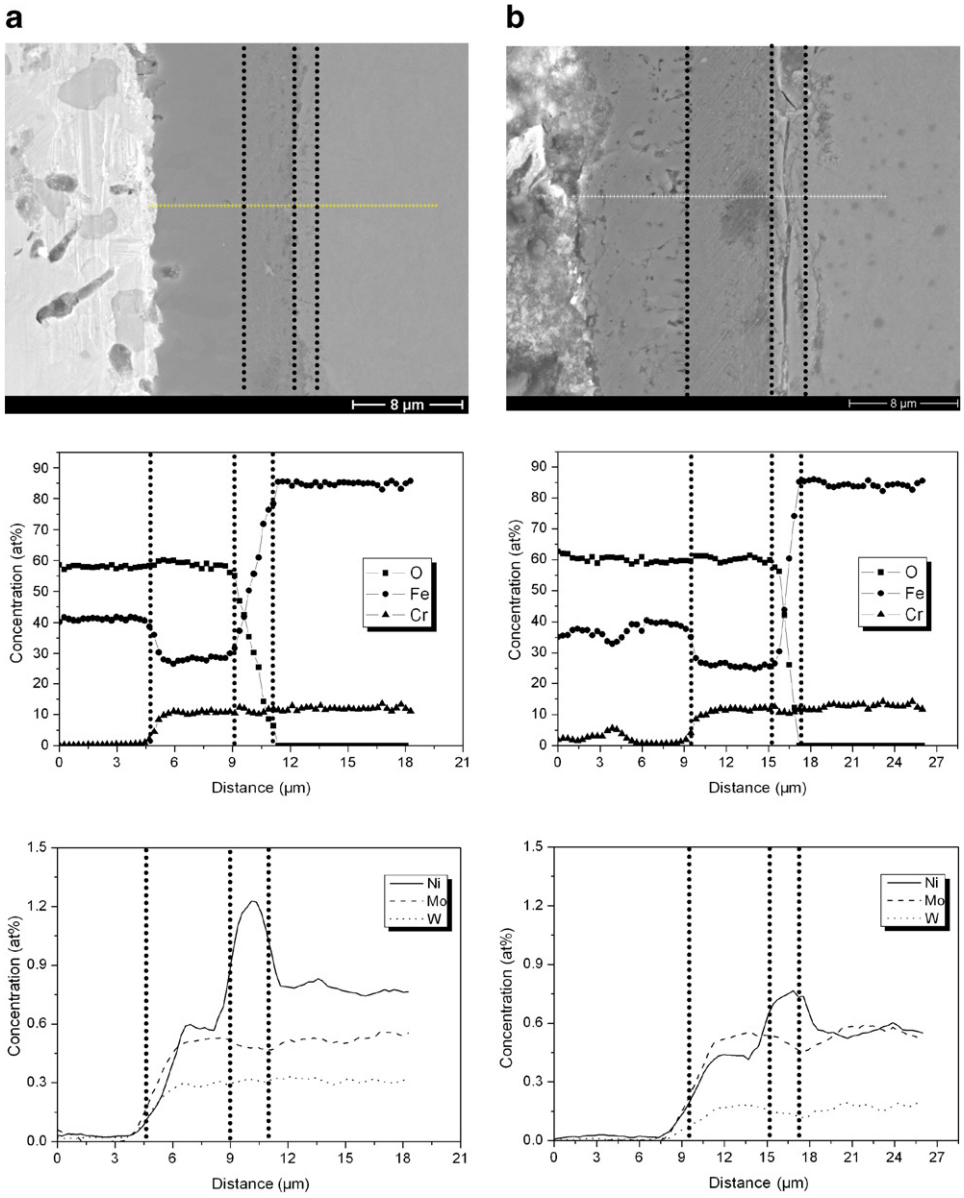

Fig. 3. SEM images of the oxide cross-section, and corresponding elemental depth profiles of untreated HT9 sample exposed to (a) 25 wppb and (b) 2 wppm dissolved oxygen content SCW at 500 °C for about 500 h. Three dashed vertical lines in each image are used to demarcate the interfaces between the outer magnetite layer, the inner spinel layer, the diffusion or internal oxidation layer, and bulk alloy successively from left to right.

SCW environment at 500 °C for 505 h. Three dominant phases were identified (indicated by different gray levels), and constituted two distinct layers in the oxide scale, which corresponded to the outer and inner oxide layer observed in the cross-section SEM images in Fig. 3. The outer oxide layer was mainly composed of magnetite, while the inner oxide layer was noted to be a mixture of spinel and ferrite. From the distribution of grain boundaries, it is observed that the outer layer consists of columnar grains perpendicular to the sample surface, and some smaller non-columnar grains close to the outer/inner oxide interface. As reported by Cory and Herrington [19] and accepted by most researchers, the interface between the two oxide layers in ferritic–martensitic steels corresponds to the original metal surface. From the viewpoint of the growth kinetics of the oxide scale, the smaller

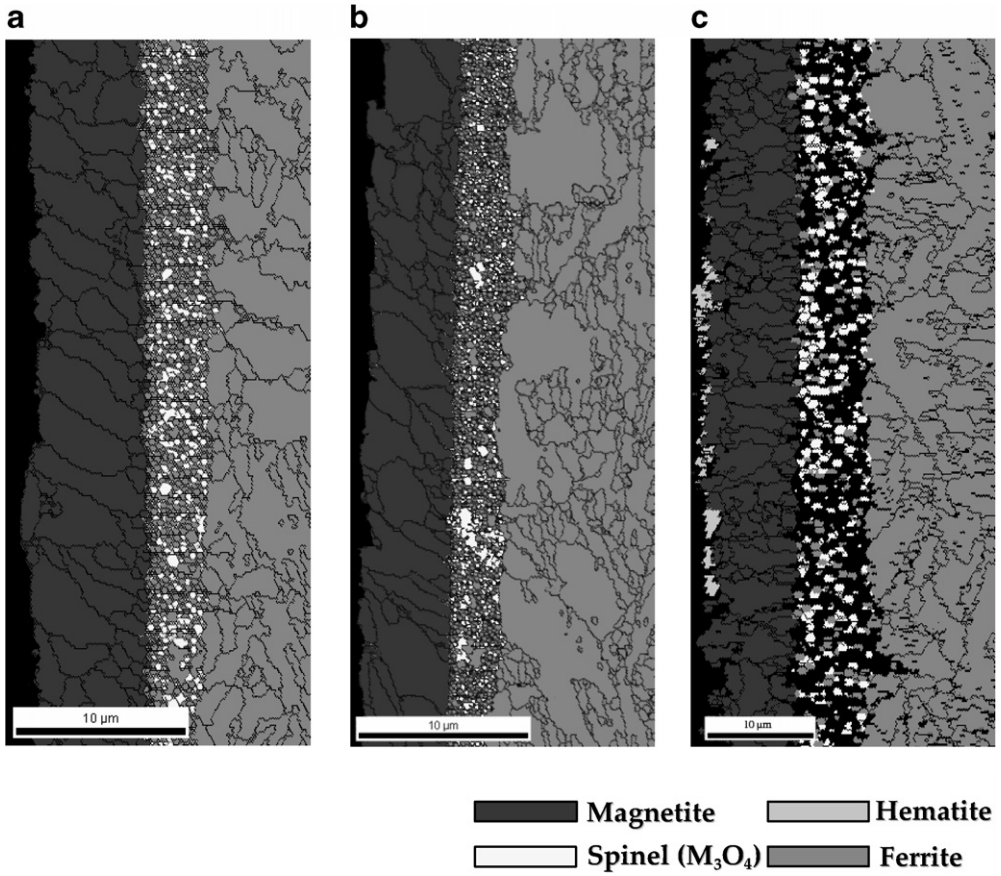

Fig. 4. Electron backscattering diffraction (EBSD) patterns for samples exposed to SCW with different dissolved oxygen contents at 500 °C after about 500 h. (a) and (b) are for untreated and surface modified samples exposed to 25 wppb SCW, respectively, and (c) is for the 2 wppm SCW exposed sample. Dominant phases, hematite, magnetite, spinel and ferrite, are indicated by different gray levels, and grain boundaries are shown by black curves. Black areas are unindexed.

grains close to the interface could be thought to form at the initial stage from the nucleation sites on the original polished sample surface. Subsequently, some of these initial grains grow larger by the reaction between dissolved oxygen and iron ions that diffuse from the bulk alloy, even at the expense of the surrounding small grains. Finally, columnar grains form along the direction by which the iron diffused from the bulk to the scale/SCW interface. As shown in Fig. 4(c), the EBSD pattern for the sample exposed to 2 wppm SCW at 500 °C for 503 h has a similar layered structure, except for a discontinuous hematite layer that forms on the outermost surface of the oxide.

The phase structures of samples exposed to SCW at different dissolved oxygen content could be confirmed by their theta–2theta XRD spectrums, as shown in Fig. 5. In the spectra for samples exposed to 25 wppb oxygen SCW, magnetite and spinel were the two phases that appeared in both untreated (Fig. 5(a)) and surface modified (Fig. 5(b)) samples. Because the crystallographic structure of spinel phase (cubic, $a = 0.8379$ nm) is nearly identical to magnetite phase (cubic, $a = 0.8396$ nm), their peaks are not readily discernable, and therefore only the standard pattern for magnetite is indicated in the figures by vertical dashed lines. More detailed analysis does show the existence of the spinel phase. In addition to the magnetite and spinel phases identified in the 25 wppb SCW exposed samples, the samples exposed to 2 wppm SCW (Fig. 5(c)) exhibited two new phases, hematite and chromium oxide (Cr_2O_3). The formation of the various oxide phases is consistent with thermodynamic calculations based on the differences in oxygen content [20].

One interesting phenomena observed for 25 wppb oxygen SCW exposed samples is that the XRD relative peak intensities of untreated samples

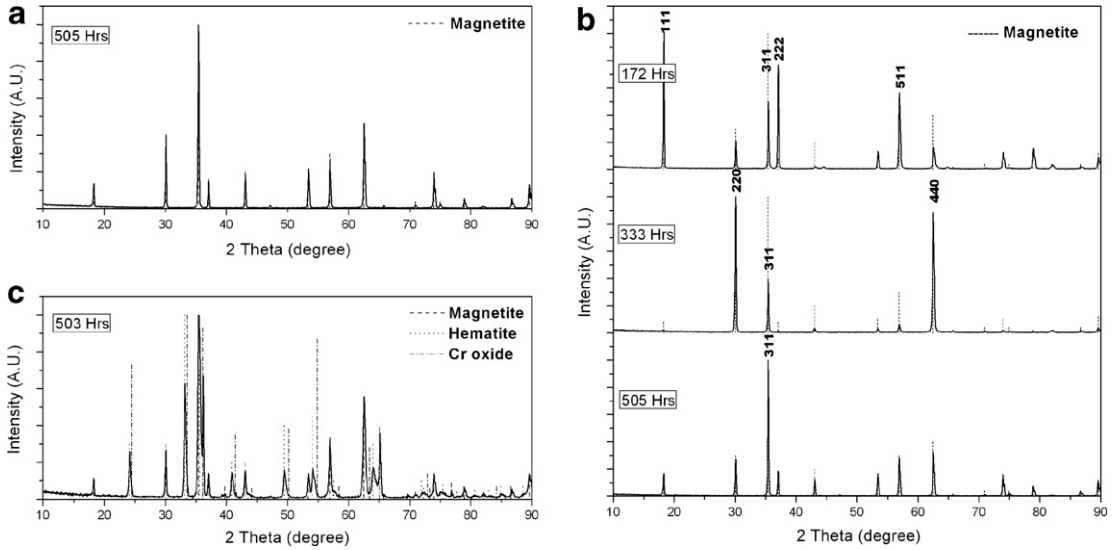

Fig. 5. X-ray diffraction patterns for 25 wppb dissolved oxygen SCW exposed HT9 samples (a) without and (b) with surface modification, and (c) for HT9 exposed to 2 wppm SCW. The standard peaks for magnetite, hematite and chromium oxide are indicated by different style lines in each pattern, where applicable. Due to the similarity of the patterns, only the samples with the longest exposure time are shown in (a) and (c).

with various exposure periods were very similar and close to those of standard magnetite. However, for surface modified samples, only the samples exposed for 505 h showed these relative peak intensities, whereas some preferred crystal orientations (texture) appeared in samples exposed to shorter exposure time (172 and 333 h), as shown in Fig. 5(b). The preferred orientations are (1 1 1) and (1 1 0) for 172- and 333-h exposed samples, respectively. This phenomenon was investigated further by using inverse pole figures (IPFs), to determine the distribution of crystal orientations. From the magnetite [0 1 0] IPFs of surface modified samples exposed to 25 wppb SCW (Fig. 6), preferred orientations are undoubtedly observed for short time exposed samples, but there is no obvious texture for the samples exposed for longest exposure times. Furthermore, the preferred crystal orientation was (1 1 1) for the 172-h exposed sample, and (1 1 0) for the 333-h exposed sample. This result is consistent with the results the XRD analysis discussed earlier. The preferred orientations formed in surface modified samples with short exposure time may reduce the oxide growth rate, and lead to a lower weight gain for longer exposure times. The texture of the oxide observed for the oxygen ion implanted samples could occur due to two possible mechanisms. The first possibility is that, among randomly orientated initial grains, some with certain crystal orientations grow faster than the others to release the stress introduced by the ion implantation or the oxide growth. The second possibility is that implantation

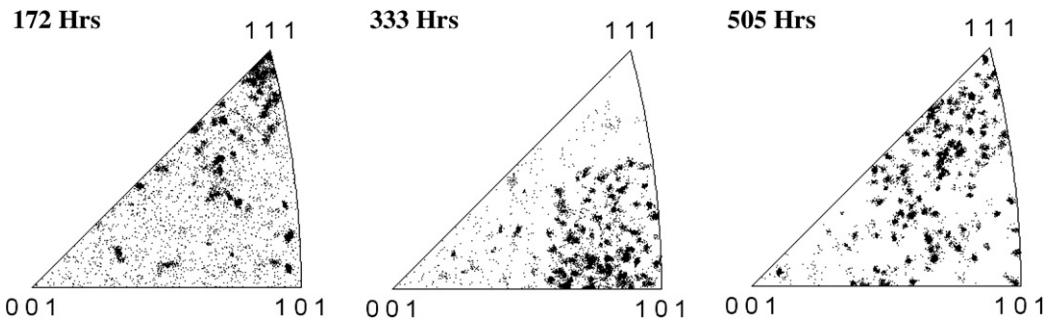

Fig. 6. Magnetite [0 1 0] inverse pole figures for surface modified samples exposed to 25 wppb dissolved oxygen SCW at 500 °C for various time periods.

of oxygen ions may increase nucleation sites with certain preferred orientations at the initial stage of oxide formation, resulting in a denser textured oxide layer. Further investigations for the mechanism of textures in surface modified samples are in progress.

4. Conclusion

A porous oxide surface was observed to develop on HT9 steel exposed to 25 wppb dissolved oxygen content SCW at 500 °C for various exposure times up to 505 h. Exposure to higher oxygen content (2 wppm) supercritical water resulted in an oxide layer with much finer grain size and the formation of Cr-rich blades on the outer surface of oxide scale. SEM cross-section images and composition depth profiles of the oxide layers on samples exposed to 25 wppb SCW indicated the presence of an Fe-rich magnetite outer oxide and a Cr-rich inner oxide that was a mixture of ferrite and spinel phases. Samples exposed to the higher 2 wppm dissolved oxygen content, developed an outermost hematite layer in addition to the magnetite and spinel layers observed for the lower oxygen content supercritical water. Oxygen implantation resulted in a slight improvement in oxidation resistance of samples in SCW with 25 wppb oxygen content at 500 °C for long-term exposure (505 h), which may be due to the development of preferred orientations in the outer oxide layer.

Disclaimer

'This report was prepared as an account of work sponsored by an agency of the United States Government. Neither the United States Government nor any agency thereof, nor any of their employees, makes any warranty, express or implied, or assumes any information, apparatus, product, or process disclosed, or represents that its use would not infringe privately owned rights. Reference herein to any specific commercial products, process, or service by trade name, trademark, manufacturer, or otherwise does not necessarily constitute or imply its endorsement, recommendation, or favoring by the United States Government or any agency thereof. The views and opinions of authors expressed herein do not necessarily state or reflect those of the United States Government or any agency thereof.'

Acknowledgements

The authors are grateful to Mark Anderson, Jeremy Licht, Yun Chen and Lizhen Tan for assisting with SCW tests and for helpful discussion. This work is supported by the Idaho National Engineering and Environmental Laboratory as part of the Department of Energy Generation IV Initiative and by the Department of Energy, Office of Nuclear Energy, Science, and Technology as part of INERI grant 2003-008-K.

References

[1] A Technology Roadmap for Generation IV Nuclear Energy Systems. US DEO Nuclear Energy Research Advisory Committee and the Generation IV International Forum, December 2002.
[2] I.G. Wright, B.A. Pint, in: Proceeding of NACE CORROSION 2002, Denver, CO, No. 02377, 2002.
[3] S. Yesodharan, Curr. Sci. 82 (2002) 1112.
[4] T.R. Allen, Workshop on Higher Temperature Materials for Advanced Nuclear Energy Systems, DOE Office of Nuclear Energy, Science and Technology, La Jolla, CA, March 18, 2002.
[5] R.L. Klueh, D.R. Harries, High-Chromium Ferritic and Martensitic Steels for Nuclear Application, American Society for Testing and Materials, West Conshohocken, PA, 2001.
[6] B. Ray, S.L. Mannan, P.R. Vasudeva Rao, M.D. Mathew, Sadhana-Acad. P. Eng. Sci. 27 (2002) 527.
[7] A. Fry, S. Osgerby, M. Wright, Oxidation of Alloys in Steam Environments – A Review, NPL Report MATC(A)90, September 2002.
[8] Y. Chen, K. Sridharan, T. Allen, in: Proceeding of NACE CORROSION 2005, Houston, TX, No. 05391, 2005.
[9] L. Tan, T. Allen, Corros. Sci., in press.
[10] J. Jang, C.H. Han, B.H. Lee, Y.S. Yi, S.S. Hwang, in: Proceeding of ICAPP 05, Seoul, Korea, No. 5136, 2005.
[11] K. Sridharan, A. Zillmer, J.R. Licht, T.R. Allen, M.H. Anderson, L. Tan, in: Proceeding of ICAPP 04, Pittsburgh, PA, No. 537, 2004.
[12] A. Atkinson, Rev. Mod. Phys. 57 (1985) 437.
[13] M. Hansel, W.J. Quadakkers, D.J. Young, Oxid. Met. 59 (2003) 285.
[14] G.E. Totten, M.A.H. Howes, Steel Heat Treatment Handbook, Marcel Dekker, New York, 1997.
[15] M. Ueda, M. Nanko, K. Kawamura, T. Maruyama, Mater. High Temp. 20 (2003) 109.
[16] R. Hales, Mater. Corros. 29 (1978) 393.
[17] G.V. Samsonov, The Oxide Handbook, IFI/Plenum Data Corporation, New York, 1973.
[18] D.J. Dingley, V. Randle, J. Mater. Sci. 27 (1992) 4545.
[19] N.J. Cory, T.M. Herrington, Oxid. Met. 28 (1987) 237.
[20] M. Schutze, Protective Oxide Scales and Their Breakdown, John Wiley, West Sussex, England, 1997.